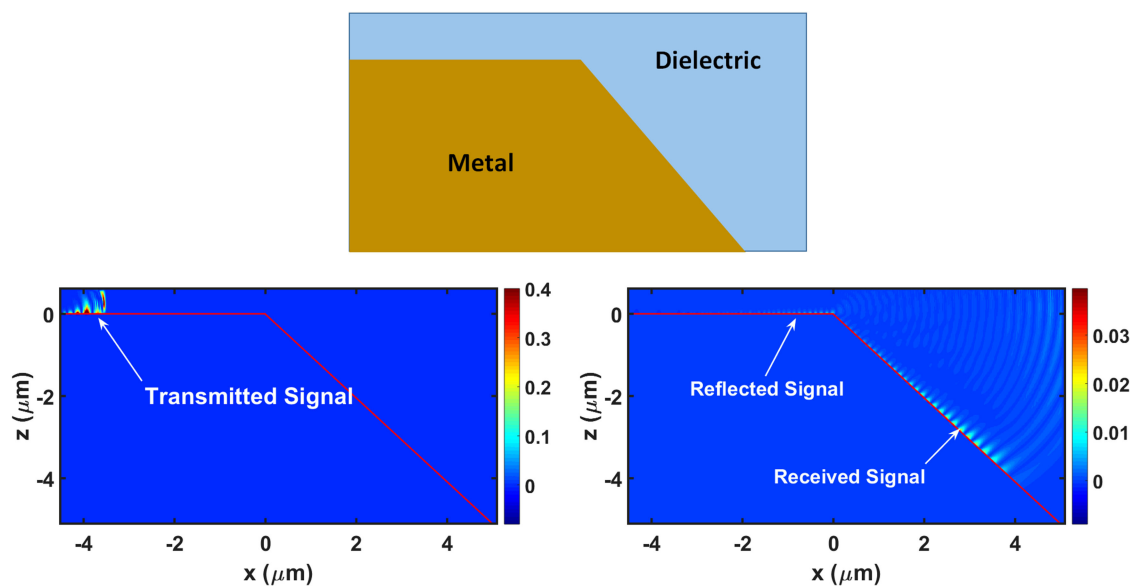


# Toward Information Transfer Around a Concave Corner by a Surface-Plasmon-Polariton Wave

Volume 11, Number 1, February 2019



Rajan Agrahari, *Student Member, IEEE*  
Akhlesh Lakhtakia, *Fellow, IEEE*  
Pradip K. Jain, *Senior Member, IEEE*



DOI: 10.1109/JPHOT.2018.2884789

1943-0655 © 2018 IEEE

# Toward Information Transfer Around a Concave Corner by a Surface-Plasmon-Polariton Wave

Rajan Agrahari <sup>1</sup>, *Student Member, IEEE*,  
Akhlesh Lakhtakia <sup>1,2</sup>, *Fellow, IEEE*,  
and Pradip K. Jain, <sup>1,3</sup> *Senior Member, IEEE*

<sup>1</sup>Material Architecture Centre and Department of Electronics Engineering, Indian Institute of Technology (BHU), Varanasi 221005, India

<sup>2</sup>Department of Engineering Science and Mechanics, Pennsylvania State University, University Park, PA 16802 USA

<sup>3</sup>Department of Electronics and Communication Engineering, National Institute of Technology, Patna, Patna 800005, India

DOI:10.1109/JPHOT.2018.2884789

1943-0655 © 2018 IEEE. Translations and content mining are permitted for academic research only. Personal use is also permitted, but republication/redistribution requires IEEE permission. See [http://www.ieee.org/publications\\_standards/publications/rights/index.html](http://www.ieee.org/publications_standards/publications/rights/index.html) for more information.

Manuscript received October 16, 2018; revised November 26, 2018; accepted November 29, 2018. Date of publication December 3, 2018; date of current version December 28, 2018. The work of A. Lakhtakia and P. K. Jain was supported by the Visiting Joint Advanced Research (VAJRA) program of the Indian Department of Science and Technology by funding their collaborative research. Corresponding author: Akhlesh Lakhtakia (e-mail: akhlesh@psu.edu).

**Abstract:** As optical interconnects employing surface-plasmon-polariton (SPP) waves are expected to enable faster communication in integrated circuits, the time-domain Maxwell equations were solved using the finite-difference time-domain method to investigate the transfer of information via a pulse-modulated carrier SPP wave around a concave corner formed by two planar metal/air interfaces. The signal is launched along the first metal/air interface and received along the second metal/air interface. The corner angle affects the intensity and the duration of the received signal, but its shape is largely independent of the corner angle of the corner. Accordingly, the signal received around the concave corner is strongly and positively correlated with the transmitted signal, a promising result for SPP-wave-based optical interconnects. The energy of the received signal varies with the frequency of the carrier SPP wave. The received signal is better correlated with the transmitted signal when the carrier frequency is higher for a fixed value of the corner angle.

**Index Terms:** Plasmonic communication, surface-plasmon-polariton wave, finite-difference time-domain method, photonics.

## 1. Introduction

As transistors get smaller, electronic chips become faster and consume less electrical energy to operate. Currently, the minimum linear dimension of silicon transistors in production is 14 nm [1], i.e., about 70 times the nominal diameter of a silicon atom. So, with the present semiconductor technology, we are getting very close to the smallest transistor possible.

Information is transferred among transistors using electrical signals, but electronic interconnects are limited by low data-transfer rate and take a long time to carry digital information to the other end of a microprocessor that may be few centimeters away [2]. Furthermore, scaling down of electronic interconnects in size is insufficient to provide the density of connections required by the increasing number density of transistors inside an electronic chip. If we use light signals instead

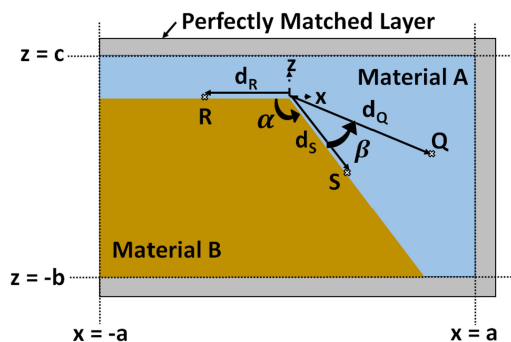


Fig. 1. Schematic of the computational domain of the initial-boundary-value problem when the metal bends to form a corner of angle  $\alpha \in (0, \pi)$ . Materials A and B are dielectric and metallic, respectively. The computational domain is bounded by three perfectly matched layers. The point labeled R is identified as the transmission point, and the point S as the reception point. Point Q is chosen for analysis of the signal scattered in the region occupied by material A beyond the corner.

of electrical signals, the data-transfer rate would be increased because photons can travel 20 times faster than electrons in a chip. However, restricted by the diffraction limit, the size of optical interconnects is approximately 1000 times larger than of transistors, this size mismatch posing a virtually insurmountable barrier. A promising solution is to use optical interconnects that exploit the phenomenon of surface-plasmon-polariton (SPP) waves [2], [3].

Quasiparticles called surface plasmons arise as collective oscillations of electrons on the naked surface of a metal illuminated by an external electromagnetic wave [4]. When vacuum (in effect, air) is replaced by a homogeneous dielectric material, quasiparticles called surface plasmon-polaritons are formed, each with a plasmonic contribution from the metal and a polaritonic contribution from the dielectric material. The classical analog of a train of SPPs is the SPP wave [5], [6]. The magnitudes of the fields of an SPP wave are maximum right at the metal/dielectric interface and decay exponentially with distance from that interface. Therefore, the fields of SPP waves are confined to lateral dimensions much smaller than the wavelength of the light. This strong localization feature of the SPP wave is promising for thin optical interconnects in semiconductor chips. As a result of strong localization, SPP-wave-based interconnects offer higher interconnect density shorter signal delay, and less crosstalk compared to electronic interconnects; energy dissipation is also less, but only for shorter transmission over short and moderate distances [7]. Furthermore, optical interconnects offer very large bandwidths in comparison to electronic interconnects [2].

With this motivation, recently we solved the Maxwell equations in the time domain to investigate the jump of a pulse-modulated carrier SPP wave across a semi-infinite gap on the metallic side of a planar metal/dielectric interface [8]. Calculations were made with air as the dielectric material and silver as the metal. The signal continued to propagate in the forward direction for a long distance after the abrupt termination of the metal, remaining strongly and positively correlated [9] with the transmitted signal. When the metal/air interface was restored after a gap of width equal to the carrier wavelength in free space, the signal received across the gap was strongly and positively correlated with the transmitted signal. These are promising result for information transfer through SPP-wave-based optical interconnects.

Not only gaps but concave corners are also common in electronic chips [11], [12]. The corners need not be right-angled, as was the case covered implicitly in the predecessor paper [8]. Accordingly, we set up the initial-boundary-value problem for information transmitted by a pulse-modulated SPP wave when the metal/dielectric interface bends abruptly to form a corner of angle  $\alpha < \pi$ ; see Fig. 1. In our formulation, the Drude model was used for the relative permittivity of the metal and the Lorentz model for that of the dielectric material [10]. The finite-difference time-domain (FDTD) method [13], [14] was used to solve the time-domain Maxwell equations in order to determine the temporal evolution of the electromagnetic field everywhere in the computational domain [8]. As all calculations were performed in the time domain, constraints imposed by boundary conditions in

frequency-domain analyses [15]–[18] were completely avoided. The Pearson correlation coefficient [9] of the appropriate component of the Poynting vector at two points, one on each of the two metal/dielectric interfaces forming the corner was calculated in order to compare the transmitted and the received signals, with air chosen as the dielectric material.

A brief description of the theoretical treatment is provided in Section 2, followed by a discussion of the obtained results in Section 3. The paper concludes with some closing remarks in Section 4.

## 2. Theory in Brief

The computational domain of the chosen initial-boundary-value problem is depicted in Fig. 1. The relevant physical domain is identified by the region  $\mathcal{R} : \{|x| \leq a, -\infty < y < \infty, -b \leq z \leq c\}$  and the relevant temporal domain as  $\mathcal{T} : \{t \geq 0\}$ . The blue region  $\mathcal{R}_A$  is occupied by a homogeneous dielectric material labeled A and the other region  $\mathcal{R}_B$  by a homogeneous metal labeled B. Both materials are chosen such that an SPP wave can travel guided by the interface  $z = 0$  at a fixed frequency  $f_c$  [4]–[6]. The horizontal and the bent metal/dielectric interfaces form a concave corner of angle  $\alpha < \pi$ . The physical domain  $\mathcal{R}$  is encapsulated by perfectly match layers (PMLs) [8], [19] above the plane  $z = c$ , below the plane  $z = -b$ , and to the right of the plane  $x = a$  in order to prevent reflection into  $\mathcal{R}$ . Even so, the dimensions  $b$  and  $c$  must be chosen to be sufficiently large that the reflections are minuscule. As material B is a metal,  $b$  should exceed the skin depth [20] at frequency  $f_c$ .

In our FDTD simulations, a pulse-modulated SPP wave is launched into the computational domain from the plane  $x = -a$  at the time  $t = 0$ . To analyze the adequacy of information transmission around the corner, we identify (i) a point labeled R ( $x_R = -d_R, z_R = 0^+$ ) on the horizontal metal/dielectric interface as the point of transmission and (ii) a point labeled S ( $x_S = -d_S \cos \alpha, z_S = -d_S \sin \alpha$ ) on the bent metal/dielectric interface as the point of reception, as shown in Fig. 1. A point labeled Q ( $x_Q = -d_Q \cos(\alpha + \beta), z_Q = -d_Q \sin(\alpha + \beta), \beta > 0$ ) is chosen in region  $\mathcal{R}_A$  for analysis of the signal scattered into material A beyond the plane  $x = 0$ . The dimension  $a$  of the computational domain is chosen keeping the propagation distance [8] of the carrier SPP wave in mind. Furthermore, the depths of penetration [8] of the carrier SPP wave in materials A and B have to be considered while deciding the dimensions  $b$  and  $c$ . All fields in this problem are independent of  $y$ .

As both materials A and B are nonmagnetic, the time-domain constitutive relations are

$$\mathbf{H}(x, z, t) = \mu_0^{-1} \mathbf{B}(x, z, t), \quad \mathbf{D}(x, z, t) = \varepsilon_0(\varepsilon_\ell \star \mathbf{E})(x, z, t), \quad (1)$$

where  $\mu_0$  and  $\varepsilon_0$  are the permeability and permittivity, respectively, of free space;  $\varepsilon_\ell(t)$  is the time-domain relative permittivity function; and the temporal-convolution operator  $\star$  [8] indicates the dispersive nature of both materials. With  $\tilde{\varepsilon}_\ell(\omega)$  denoting the temporal Fourier transform of  $\varepsilon_\ell(t)$ , where  $\omega$  is the angular frequency, we chose the Lorentz model [10]

$$\tilde{\varepsilon}_A(\omega) = 1 + \left\{ \frac{\rho_A \Omega_A}{\Omega_A^2 \left[ 1 + (2\pi N_A)^{-2} \right] - \omega^2 - i\omega \Omega_A / \pi N_A} \right\} \quad (2)$$

for the dielectric material and the Drude model [21], [22]

$$\tilde{\varepsilon}_B(\omega) = 1 - \left[ \frac{\omega_B^2}{\omega(\omega + i/\tau_B)} \right] \quad (3)$$

for the metal. The constants  $\rho_A$ ,  $\Omega_A$ , and  $N_A$  quantify the oscillator strength, resonance wavelength, and linewidth of material A, whereas  $\omega_B$  and  $\tau_B$ , respectively, are the plasma angular frequency and relaxation time of material B. The inverse Fourier transform yields [23], [24]

$$\varepsilon_A(t) = \delta(t) + \rho_A \Omega_A \exp\left(-\frac{\Omega_A t}{2\pi N_A}\right) \sin(\Omega_A t) \mathcal{U}(t) \quad (4)$$

and

$$\varepsilon_B(t) = \delta(t) + \omega_B^2 \tau_B \left[ 1 - \exp\left(-\frac{t}{\tau_B}\right) \right] \mathcal{U}(t), \quad (5)$$

where  $\delta(t)$  is the Dirac delta.

For the FDTD simulations,  $\partial/\partial y \equiv 0$  is set in the time-domain Maxwell curl equations, leading to

$$\left. \begin{aligned} \partial_t D_x(x, z, t) &= -\partial_z H_y(x, z, t) \\ \partial_t D_z(x, z, t) &= \partial_x H_y(x, z, t) \\ \partial_t H_y(x, z, t) &= \mu_0^{-1} [\partial_x E_z(x, z, t) - \partial_z E_x(x, z, t)] \end{aligned} \right\}, \quad (6)$$

where  $\partial_w \equiv \partial/\partial w$ . After defining the time-domain susceptibility function  $\chi_\ell(t) = \varepsilon_\ell(t) - \delta(t)$ , the FDTD updating equations can be obtained by applying the central-difference formula [25] to Eqs. (6) [13].

With  $\mathcal{R}$  discretized into  $m\Delta x \times n\Delta z$  rectangular cells and  $\mathcal{T}$  into  $p\Delta t$  linear cells, we get [8], [26],

$$\begin{aligned} E_x^{p+1}(m, n) &= E_x^p(m, n) - \frac{\Delta t}{\varepsilon_0 \Delta z} \left[ H_y^{p+\frac{1}{2}}(m, n) - H_y^{p+\frac{1}{2}}(m, n-1) \right] - \chi^p(m, n) E_x^1(m, n) \Delta t \\ &\quad - \Delta t \sum_{k=1}^{p-1} \left[ \chi^k(m, n) \{ E_x^{p-k+1}(m, n) - E_x^{p-k}(m, n) \} \right], \end{aligned} \quad (7)$$

$$\begin{aligned} E_z^{p+1}(m, n) &= E_z^p(m, n) + \frac{\Delta t}{\varepsilon_0 \Delta x} \left[ H_y^{p+\frac{1}{2}}(m, n) - H_y^{p+\frac{1}{2}}(m-1, n) \right] - \chi^p(m, n) E_z^1(m, n) \Delta t \\ &\quad - \Delta t \sum_{k=1}^{p-1} \left[ \chi^k(m, n) \{ E_z^{p-k+1}(m, n) - E_z^{p-k}(m, n) \} \right], \end{aligned} \quad (8)$$

and

$$\begin{aligned} H_y^{p+\frac{1}{2}}(m, n) &= H_y^{p-\frac{1}{2}}(m, n) + \frac{\Delta t}{\mu_0 \Delta x} [E_z^p(m+1, n) - E_z^p(m, n)] \\ &\quad - \frac{\Delta t}{\mu_0 \Delta z} [E_x^p(m, n+1) - E_x^p(m, n)]. \end{aligned} \quad (9)$$

Here, the integers  $m$ ,  $n$ , and  $p$  represent  $m\Delta x$ ,  $n\Delta z$ , and  $p\Delta t$ , respectively, and

$$\chi^p(m, n) = \begin{cases} \chi_A(p\Delta t), & m\Delta x \hat{\mathbf{u}}_x + n\Delta z \hat{\mathbf{u}}_z \in \mathcal{R}_A, \\ \chi_B(p\Delta t), & m\Delta x \hat{\mathbf{u}}_x + n\Delta z \hat{\mathbf{u}}_z \in \mathcal{R}_B, \end{cases} \quad (10)$$

Implementation details of the FDTD updating equations and the incorporation of the PMLs are available elsewhere [8].

The incident signal at  $x = -a$  is taken to be a pulse function that modulates the field amplitudes of the carrier SPP wave of angular frequency  $\omega_c = 2\pi f_c$ . Thus, the electric field on the plane  $x = -a$  for all  $t \in \mathcal{T}$  is specified as [8]

$$\mathbf{E}(-a, z, t) = \begin{cases} g(t) \operatorname{Re} [\tilde{\mathbf{E}}_A(0, z) \exp(-i\omega_c t)], & z > 0, \\ g(t) \operatorname{Re} [\tilde{\mathbf{E}}_B(0, z) \exp(-i\omega_c t)], & z < 0, \end{cases} \quad (11)$$

with

$$g(t) = \omega_c t \exp(-\omega_c t) \quad (12)$$

as the pulse function. Here, the electric field phasor of the carrier SPP wave is given by [4], [6]

$$\tilde{\mathbf{E}}_A(x, z) = \left[ \frac{-\alpha_{cA} \hat{\mathbf{u}}_x + q_c \hat{\mathbf{u}}_z}{k_c \tilde{\varepsilon}_A(\omega_c)} \right] \exp [i(q_c x + \alpha_{cA} z)] \quad (13)$$

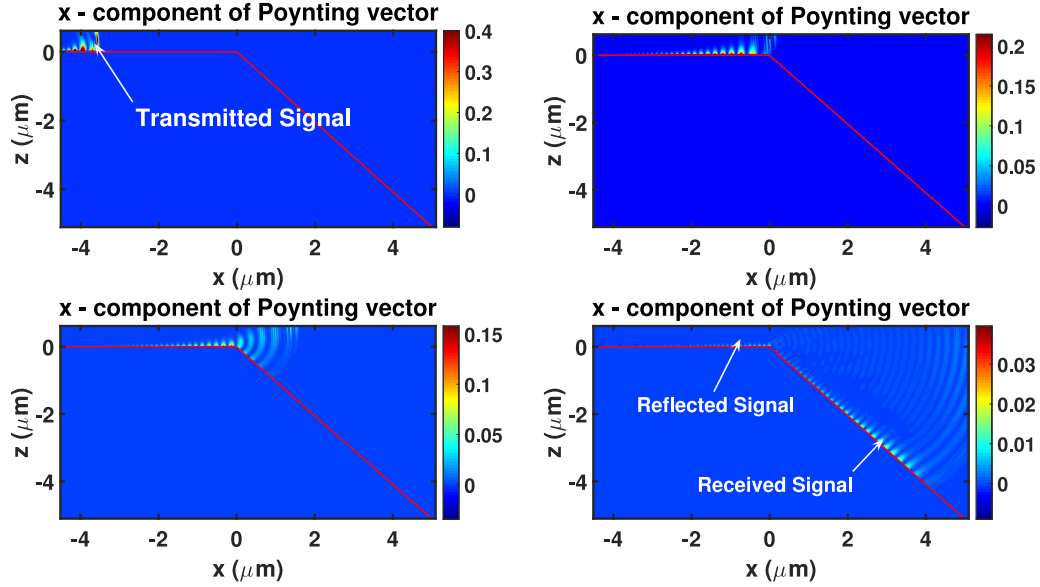


Fig. 2. Four snapshots of normalized  $P_x(x, z, t)$  taken at (top left)  $t = 4.94$  fs, (top right)  $t = 17.26$  fs, (bottom left)  $t = 21.96$  fs, and (bottom right)  $t = 37.41$  fs, when  $\lambda_c = 500$  nm and  $\alpha = 135^\circ$ . Multiply by  $1.1375 \times 10^{-4} \text{ Wm}^{-2}$  to obtain unnormalized  $P_x(x, z, t)$ .

and

$$\tilde{\mathbf{E}}_B(x, z) = \left[ \frac{\alpha_{c_B} \hat{\mathbf{u}}_x + q_c \hat{\mathbf{u}}_z}{k_c \tilde{\epsilon}_B(\omega_c)} \right] \exp [i (q_c x - \alpha_{c_B} z)], \quad (14)$$

where  $k_c = \omega_c / c_0$  is the free-space wavenumber with  $c_0$  as the speed of light in free space;  $\alpha_{cl} = \sqrt{k_c^2 \tilde{\epsilon}_l(\omega_c) - q_c^2}$  is the complex wavenumber describing field variation in the  $z$  direction;

$$q_c = k_c \sqrt{\frac{\tilde{\epsilon}_A(\omega_c) \tilde{\epsilon}_B(\omega_c)}{\tilde{\epsilon}_A(\omega_c) + \tilde{\epsilon}_B(\omega_c)}} \quad (15)$$

is the complex SPP wavenumber; and the conditions  $\text{Re}(q_c) \text{Im}(q_c) > 0$  and  $\text{Im}(\alpha_{cl}) > 0$  apply. The companion expression for  $\mathbf{H}(-a, z, t)$  for all  $t \in \mathcal{T}$  is available in the predecessor paper [8].

### 3. Numerical Results and Discussion

For all numerical results presented here, we chose material A to be air that was approximated as free space or vacuum by setting  $p_A = 0$ . Material B was chosen to be bulk silver with  $\omega_B = 1.352 \times 10^{16} \text{ rad s}^{-1}$  and  $\tau_B = 17 \times 10^{-15} \text{ s}$  [22]. FDTD simulations were undertaken with the following parameters:  $a = 5000$  nm,  $b = 5000$  nm,  $\Delta x = \Delta z = 10$  nm, and  $\Delta t = 0.022$  fs. Furthermore, we set  $c \in \{318, 524, 775, 1073\}$  nm for  $\lambda_c \in \{400, 500, 600, 700\}$  nm, where the free-space wavelength  $\lambda_c = 2\pi/k_c$ .

The phenomenon under investigation is illustrated by the four snapshots in Fig. 2 showing the spatiotemporal variation of the  $x$ -directed component of the *instantaneous* Poynting vector  $\mathbf{P}(x, z, t) = \mathbf{E}(x, z, t) \times \mathbf{H}(x, z, t)$  for  $\lambda_c = 500$  nm and  $\alpha = 135^\circ$ . The pulse-modulated carrier SPP wave is launched at  $t = 0$  from the plane  $x = -a$ . The snapshots of  $P_x(x, z, t) = \hat{\mathbf{u}}_x \bullet \mathbf{P}(x, z, t)$  are taken at  $t \in \{4.94, 17.26, 21.96, 37.41\}$  fs. The transmitted signal can be clearly seen in the first snapshot ( $t = 4.94$  fs). Arriving in the vicinity of the plane  $x = 0$ , the signal encounters the concave corner of angle  $\alpha$ , as depicted in the second snapshot ( $t = 17.26$  fs). As a result, the signal is: (i) partly reflected along the horizontal metal/dielectric interface, (ii) partly guided along the bent metal/dielectric interface, and (iii) partly scattered into the region  $\mathcal{R}_A$  to the right of the plane  $x = 0$ ,

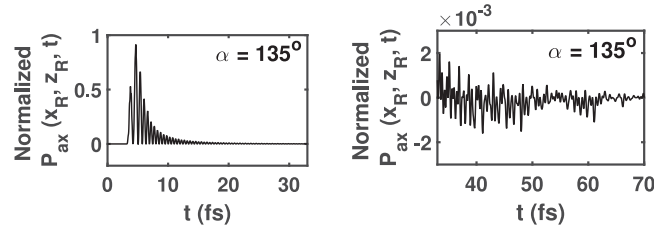


Fig. 3. Temporal profile of normalized  $P_{ax}(x_R, z_R, t)$  when  $d_R = 8\lambda_c$ ,  $\lambda_c = 500$  nm, and  $\alpha = 135^\circ$ . The transmitted signal (left) and the reflected signal (right) at point R are sufficiently separated from each other in time to be distinctly identified. Multiply by  $1.1375 \times 10^{-4} \text{ Wm}^{-2}$  to obtain unnormalized  $P_{ax}(x_R, z_R, t)$ .

as shown in the third and the fourth snapshots ( $t = 21.96$  and  $37.41$  fs). All plots of the components of the instantaneous Poynting vector in this paper are normalized with respect to the magnitude  $1.1375 \times 10^{-4} \text{ Wm}^{-2}$ . This normalization factor was computed by integrating  $P_x(-a^+, 0^+, t)$  with respect to  $t$  from 0 to 70 fs when  $\lambda_c = 500$  nm, and then dividing the result by the duration for which  $P_x(-a^+, 0^+, t)$  was at least 50% of its peak value.

### 3.1 Effect of Corner Angle on Information Transmission

With a view to ascertaining the effect of the corner angle  $\alpha$  on the signal received at S, we fixed the carrier wavelength  $\lambda_c = 500$  nm and varied  $\alpha$  from  $75^\circ$  to  $180^\circ$ . The temporal profile of the axial component of the Poynting vector

$$P_{ax}(x_R, z_R, t) = \hat{\mathbf{u}}_x \bullet \mathbf{P}(x_R, z_R, t) \quad (16)$$

at the transmission point R on the horizontal metal/dielectric interface is shown in Fig. 3 for  $\alpha = 135^\circ$  when  $d_R = 8\lambda_c$ . The left panel of the figure shows  $P_{ax}(x_R, z_R, t)$  for  $t \in [0, 33]$  fs and the right panel for  $t \in [33, 70]$  fs. The transmitted signal at point R is evident for  $t \in [3.3, 15.4]$  fs, and the reflected signal at the same point begins to appear at  $t \simeq 34$  fs. The intensity of the reflected signal is very weak, almost in the noise level when compared with the transmitted signal, which indicates that most of the energy of the transmitted signal is scattered by the concave corner with some of it possibly propagating guided by the bent metal/dielectric interface.

The dependence of the reflected signal at point R on the corner angle  $\alpha$  can be gleaned from the plots of  $P_{ax}(x_R, z_R, t)$  vs.  $t \in [33, 70]$  fs for  $d_R = 8\lambda_c$  and  $\alpha \in \{75^\circ, 90^\circ, 120^\circ, 135^\circ, 150^\circ, 180^\circ\}$  in Fig. 4. Even though the reflected signal in Fig. 4 is significantly weaker than the transmitted signal (shown in the left panel of Fig. 3) regardless of the value of  $\alpha$ , the reflected signal is definitely stronger when  $\alpha$  is acute than when  $\alpha$  is obtuse. As  $\alpha$  increases, the reflected signal weakens. Since there is no discontinuity at  $\{x = 0, z = 0\}$  when  $\alpha = 180^\circ$ , zero reflection must occur; indeed, that is borne out by the absence of negative values of  $P_{ax}$  in the bottom right panel of Fig. 4. Therefore, the vast majority of the transmitted signal is either scattered in material A (air) or is propagated along the bent metal/dielectric interface, when  $\alpha < 180^\circ$ .

The signal received at the reception point S also depends on the corner angle  $\alpha$ . The temporal profile of the axial component of the Poynting vector

$$P_{ax}(x_S, z_S, t) = -(\hat{\mathbf{u}}_x \cos \alpha + \hat{\mathbf{u}}_z \sin \alpha) \bullet \mathbf{P}(x_S, z_S, t) \quad (17)$$

at point S on the bent metal/dielectric interface is shown in Fig. 5 for  $d_S = 5\lambda_c$  and  $\alpha \in \{75^\circ, 90^\circ, 120^\circ, 135^\circ, 150^\circ, 180^\circ\}$ . The intensity of the received signal is low for  $\alpha = 75^\circ$ , but it increases monotonically as  $\alpha$  increases to  $180^\circ$ . This increase is consistent with the decrease of the intensity of the reflected signal at R in Fig. 4. However, since the reflected signal is weak for all values of  $\alpha$  in Fig. 4, the energy of the signal scattered in  $\mathcal{R}_A$  beyond the plane  $x = 0$  must decrease as  $\alpha$  increases, in accordance with the principle of conservation of energy.

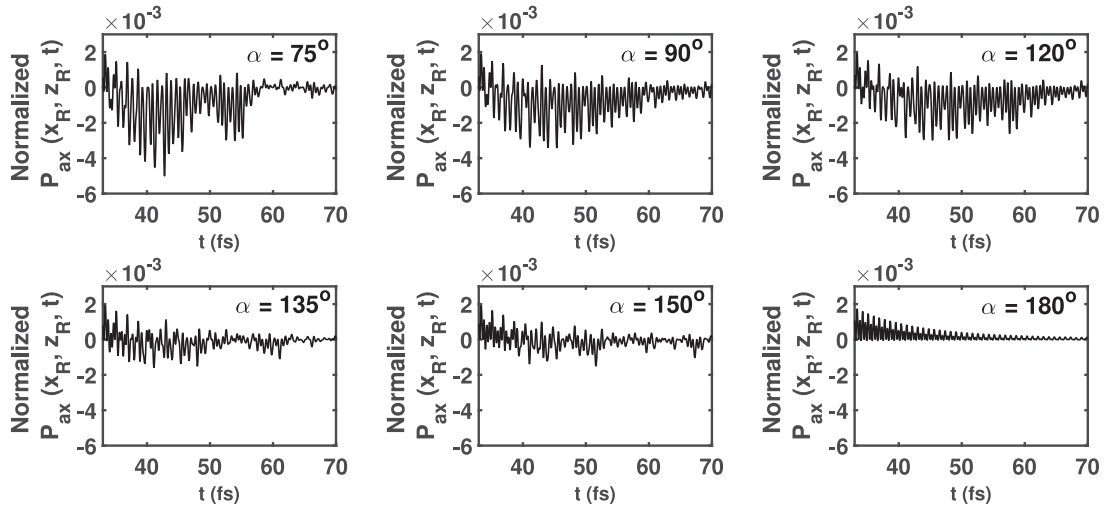


Fig. 4. Temporal profile of normalized  $P_{ax}(x_R, z_R, t)$  when  $d_R = 8\lambda_c$ ,  $\lambda_c = 500$  nm, and  $\alpha \in \{75^\circ, 90^\circ, 120^\circ, 135^\circ, 150^\circ, 180^\circ\}$ . Each profile is of the reflected signal at point R. Multiply by  $1.1375 \times 10^{-4} \text{ Wm}^{-2}$  to obtain unnormalized  $P_{ax}(x_R, z_R, t)$ .

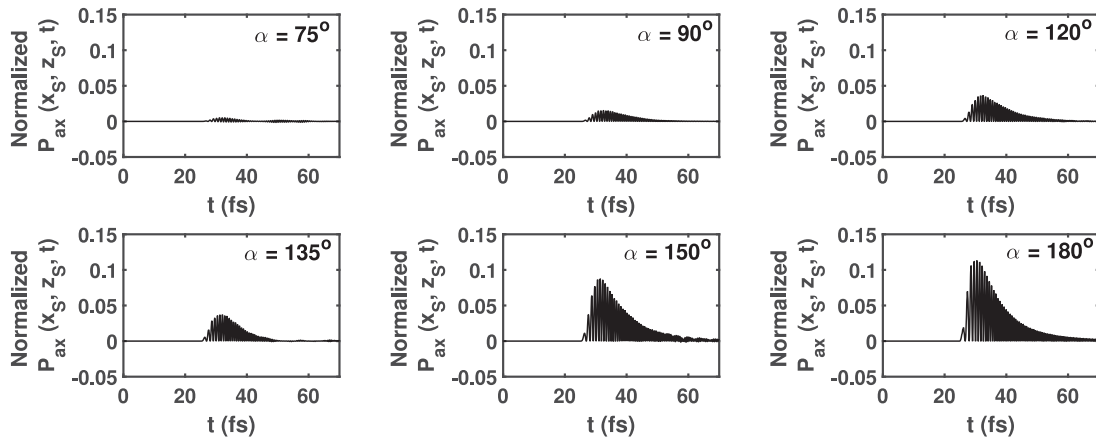


Fig. 5. Temporal profile of normalized  $P_{ax}(x_S, z_S, t)$  when  $d_S = 5\lambda_c$ ,  $\lambda_c = 500$  nm, and  $\alpha \in \{75^\circ, 90^\circ, 120^\circ, 135^\circ, 150^\circ, 180^\circ\}$ . Each profile is of the received signal at point S. Multiply by  $1.1375 \times 10^{-4} \text{ Wm}^{-2}$  to obtain unnormalized  $P_{ax}(x_R, z_R, t)$ .

For all values of  $\alpha$  in Fig. 5, the shape of the received pulse is approximately the same as that of the transmitted pulse at R (shown in the left panel of Fig. 3). No appreciable precursor has developed because the launching plane  $x = -a$  is quite close to the corner. We have verified that when  $a$  is considerably higher, a precursor [8] does develop. Nevertheless, the received signal is distorted in comparison to the transmitted signal.

If we quantify the duration of the received signal as the time interval for which  $P_{ax}(x_S, z_S, t)$  exceeds 50% of its peak value, the received signal's duration is  $\{7.91, 11.65, 10.5, 10.41, 10.3, 10.1\}$  fs for  $\alpha \in \{75^\circ, 90^\circ, 120^\circ, 135^\circ, 150^\circ, 180^\circ\}$ . The signal duration at S is approximately constant at 10.3 fs when  $\alpha$  is obtuse but decreases when  $\alpha$  is acute. The analogously defined duration of the transmitted signal in the left panel of Fig. 3 is 2.3 fs. The increasing signal duration at the reception point S compared to that of the signal transmitted at point R indicates that the pulse broadens as it propagates on the metal/air interface. This observation is consistent with different spectral components of the transmitted signal having different phase speeds [8].



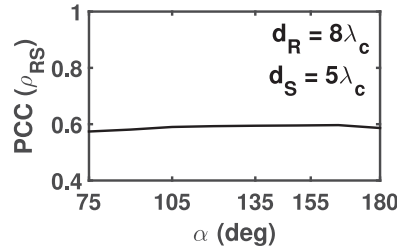


Fig. 6. Pearson correlation coefficient  $\rho_{RS}$  between  $P_{ax}(x_R, z_R, t)$  and  $P_{ax}(x_S, z_S, t)$  as a function of  $\alpha \in [75^\circ, 180^\circ]$  when  $d_R = 8\lambda_c$ ,  $d_S = 5\lambda_c$ , and  $\lambda_c = 500$  nm.

A comparison of the left panel of Fig. 3 with the bottom right panel of Fig. 5 shows that the energy of the signal weakens as it travels along a planar metal/dielectric interface, in agreement with the predecessor paper [8]. This because of attenuation of the carrier SPP wave [6] due to the metal being dissipative [21].

In order to quantify the similarity of the signal received at point S to the signal transmitted at point R, we determined the Pearson correlation coefficient  $\rho_{RS} \in [-1, 1]$  [9] between the received and the transmitted signals. This coefficient is defined as [8]

$$\rho_{RS} = \frac{\sum_{\ell=1}^N [\Delta P_{ax}(x_R, z_R, t_\ell) \cdot \Delta P_{ax}(x_S, z_S, t_\ell - \bar{t})]}{\sqrt{\left\{ \sum_{\ell=1}^N [\Delta P_{ax}(x_R, z_R, t_\ell)]^2 \right\}} \cdot \sqrt{\left\{ \sum_{\ell=1}^N [\Delta P_{ax}(x_S, z_S, t_\ell - \bar{t})]^2 \right\}}}, \quad (18)$$

where

$$\Delta P_{ax}(x, z, t_\ell) = P_{ax}(x, z, t_\ell) - \frac{1}{N} \sum_{k=1}^N P_{ax}(x, z, t_k) \quad \ell \in [1, N], \quad (19)$$

and  $\bar{t}$  is the time of flight of a plane wave in vacuum across the distance between the points of transmission and reception.

The Pearson correlation coefficient correlates the shapes of the transmitted and received signals, with positive values indicating correlation and negative values indicating lack of correlation. The closer that  $|\rho_{RS}|$  is to unity, the stronger is the correlation or anticorrelation, as indicated by the sign of  $\rho_{RS}$ . If the received signal is independent of the transmitted signal, then  $\rho_{RS} = 0$ . Thus, the Pearson correlation coefficient is a simple, but not comprehensive, measure of the fidelity of information transfer.

Figure 6 shows the variation of  $\rho_{RS}$  with  $\alpha \in [75^\circ, 180^\circ]$  when  $d_R = 8\lambda_c$  and  $d_S = 5\lambda_c$ . Since the shape of the received signal is approximately the same as that of the transmitted signal, as indicated by Figs. 3 and 5,  $\rho_{RS} = 0.585 \pm 0.015$  over the chosen range of  $\alpha$ , thereby confirming that the shape of the signal received at S is largely independent of the corner angle of the corner. However,  $\rho_{RS}$  does not have higher values since the duration of the received signal is different from that of the transmitted signal. The high and positive values of  $\rho_{RS}$  also indicate that information can indeed be transferred by a carrier SPP wave around a concave corner.

### 3.2 Effect of Carrier Wavelength on Information Transmission

In order to study the effect of the carrier wavelength  $\lambda_c$  on information transfer, we used Eq. (15) to plot the dispersion diagram in Fig. 7 for an SPP wave guided by the silver/air interface. The phase speed  $\omega_c/\text{Re}(q_c)$  is higher but the attenuation rate  $\text{Im}(q_c)$  is lower for larger  $\lambda_c$ .

Next, we fixed  $\alpha = 135^\circ$  but varied  $\lambda_c \in \{400, 500, 600, 700\}$  nm. The temporal profiles of  $P_{ax}(x_R, z_R, t)$  at the transmission point R are shown in Fig. 8 when  $d_R = 5\lambda_c$ . The peak intensity of the transmitted signal at point R increases as  $\lambda_c$  increases. Fig. 9 shows the corresponding temporal profiles of  $P_{ax}(x_S, z_S, t)$  (at the reception point S) calculated with  $d_S = 5\lambda_c$ . A comparison

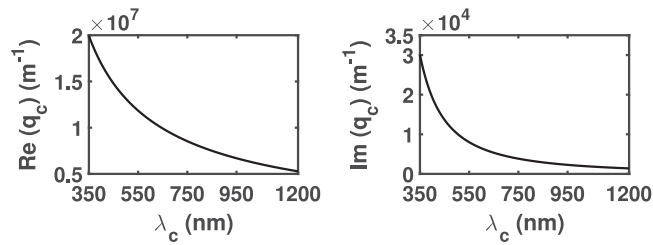


Fig. 7. Real and imaginary parts of the SPP wavenumber  $q_c$  as functions of carrier wavelength  $\lambda_c$ .

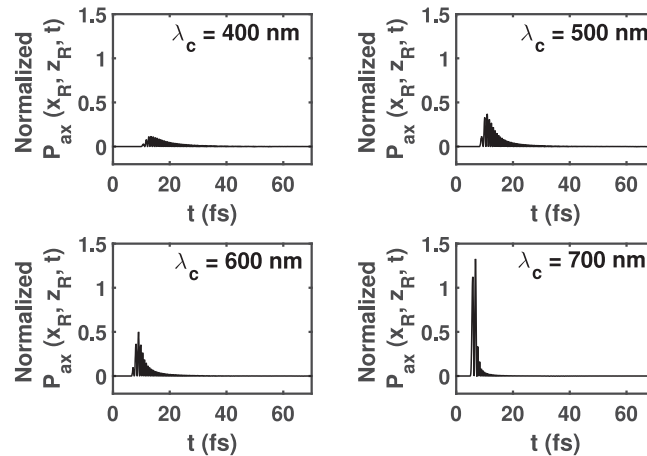


Fig. 8. Temporal profile of normalized  $P_{ax}(x_R, z_R, t)$  when  $d_R = 5\lambda_c$ ,  $\lambda_c \in \{400, 500, 600, 700\}$  nm, and  $\alpha = 135^\circ$ . Each profile is of the transmitted signal at point R. Multiply by  $1.1375 \times 10^{-4} \text{ Wm}^{-2}$  to obtain unnormalized  $P_{ax}(x_R, z_R, t)$ .

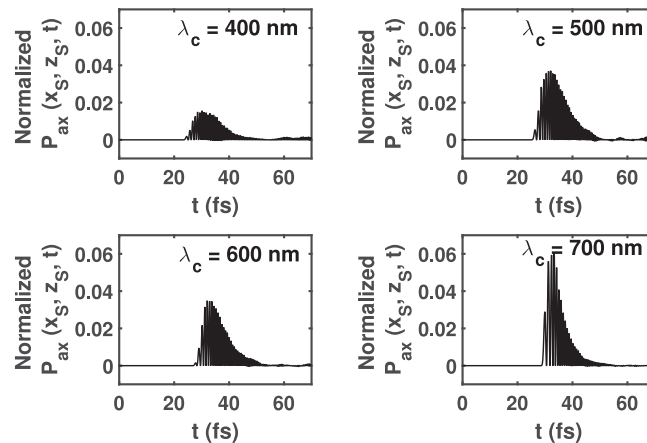


Fig. 9. Temporal profile of normalized  $P_{ax}(x_S, z_S, t)$  when  $d_R = 5\lambda_c$ ,  $d_S = 5\lambda_c$ ,  $\lambda_c \in \{400, 500, 600, 700\}$  nm, and  $\alpha = 135^\circ$ . Each profile is of the received signal at point S. Multiply by  $1.1375 \times 10^{-4} \text{ Wm}^{-2}$  to obtain unnormalized  $P_{ax}(x_S, z_S, t)$ .

of the four profiles in this figure indicates that the peak intensity of the received signal increases as  $\lambda_c$  increases, in part because of the higher peak of the transmitted signal (Fig. 8), and in part because the attenuation rate of the carrier SPP wave decreases as  $\lambda_c$  increases [8].

Furthermore, the shape of the received signal at point S is about the same as that of the transmitted signal at point R, although pulse broadening occurs for every  $\lambda_c \in \{400, 500, 600, 700\}$  nm. However, the transmitted signal's duration at point R and the received signal's duration at point S

TABLE 1  
 $\rho_{RS}$  in Relation to  $\lambda_c$  When  $d_R = 5\lambda_c$ ,  $d_S = 5\lambda_c$ , and  $\alpha = 135^\circ$

Carrier wavelength $\lambda_c$ (nm)	Pearson correlation coefficient $\rho_{RS}$
400	0.7642
500	0.7545
600	0.7278
700	0.6683

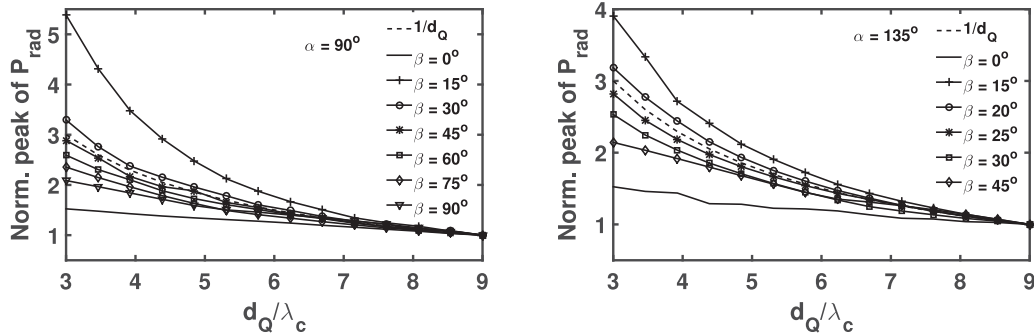


Fig. 10. Normalized peak intensity of  $P_{\text{rad}}(x_Q, z_Q, t)$  as a function of  $d_Q/\lambda_c \in [3, 9]$  with  $\lambda_c = 500$  nm fixed. Left:  $\alpha = 90^\circ$  and  $\beta \in \{0^\circ, 90^\circ\}$ . Right:  $\alpha = 135^\circ$  and  $\beta \in \{0^\circ, 45^\circ\}$ . The peak intensity for each value of  $\beta$  is normalized to unity for  $d_Q = 9\lambda_c$ . The normalized curve for the  $1/d_Q$  dependence is also shown.

are markedly lower for  $\lambda_c = 700$  nm than for the other three values of  $\lambda_c$ . Quantified as the time interval for which  $P_{\text{ax}}$  exceeds 50% of its peak value, the duration of the transmitted signal in Fig. 8 is {6.49, 3.90, 2.59, 1.50} fs for  $\lambda_c \in \{400, 500, 600, 700\}$  nm. Correspondingly, the duration of the received signal in Fig. 9 is {11.53, 10.41, 9.31, 5.68} fs. Thus, pulse broadening continues to occur on the metal/air interface after the signal has gone around the concave corner.

Table 1 shows the variation of  $\rho_{RS}$  with  $\lambda_c$  for  $d_R = 5\lambda_c$  and  $d_S = 5\lambda_c$ , when  $\alpha = 135^\circ$ . As  $\lambda_c$  increases from 400 to 700 nm,  $\rho_{RS}$  reduces from 0.76 to 0.67. Thus the received signal is better correlated with the transmitted signal when the carrier wavelength  $\lambda_c$  is lower.

We conclude that the energy content of the received signal increases but the shape and duration of the received signal differ more from those of the transmitted signal, as  $\lambda_c$  increases.

### 3.3 Scattered Signal

The signal arriving at the concave corner not only travels along the bent metal/dielectric interface but is also scattered into the region  $\mathcal{R}_A$  to the right of the plane  $x = 0$ . In order to determine the dependency of the scattered field on the radial distance from the corner  $\{x = 0, y = 0\}$ , we focused our attention on point Q identified in Fig. 1 and computed the radial component

$$P_{\text{rad}}(x_Q, z_Q, t) = -[\hat{\mathbf{u}}_x \cos(\alpha + \beta) + \hat{\mathbf{u}}_z \sin(\alpha + \beta)] \cdot \mathbf{P}(x_Q, z_Q, t) \quad (20)$$

of the instantaneous Poynting vector as a function of the distance  $d_Q$ .

Focusing at distances far from the corner, we varied  $d_Q/\lambda_c \in [3, 9]$  for  $\lambda_c = 500$  nm. The dependency of the scattered field on the radial distance was determined for two representative cases:

- $\alpha = 90^\circ$  and  $\beta \in \{0^\circ, 90^\circ\}$  and
- $\alpha = 135^\circ$  and  $\beta \in \{0^\circ, 45^\circ\}$ .

Figure 10 presents the peak intensity of the temporal profile of  $P_{\text{rad}}(x_Q, z_Q, t)$  as a function of  $d_Q$  for both cases. In order to facilitate comparison, the peak intensity for each value of  $\beta$  is normalized to unity for  $d_Q = 9\lambda_c$ . Also plotted is a similarly normalized curve for the  $1/d_Q$  dependence.

As  $d_Q$  increases, the peak intensity of  $P_{\text{rad}}(x_Q, z_Q, t)$  decreases as  $1/d_Q^\gamma$  for every value of  $\beta$  in Fig. 10. When  $\alpha = 90^\circ$ ,  $\gamma \simeq 1$  for  $\beta \in [30^\circ, 90^\circ]$ ,  $\gamma \simeq 1.5$  for  $\beta = 15^\circ$ , and  $\gamma \simeq 0.5$  for  $\beta = 0^\circ$  in Fig. 10(left). Similarly, when  $\alpha = 135^\circ$ ,  $\gamma \simeq 1$  for  $\beta \in [20^\circ, 45^\circ]$ ,  $\gamma \simeq 1.4$  for  $\beta = 15^\circ$ , and  $\gamma \simeq 0.5$  for  $\beta = 0^\circ$  in Fig. 10(right). According to the Huygens principle for two-dimensional frequency-domain electromagnetics, electromagnetic field phasors vary as  $1/d_Q^{0.5}$  and the time-averaged Poynting vector as  $1/d_Q$  in the far zone [27], [28]. Thus, proximity to the bent metal/dielectric interface affects the scattered signal in the region  $\mathcal{R}_A$  beyond the plane  $x = 0$ .

## 4. Conclusion

We solved the time-domain Maxwell equations using the FDTD method to investigate the transfer of information via a pulse-modulated carrier SPP wave around a concave corner formed by two planar metal/air interfaces. Launched along the first metal/air interface, the signal is partly reflected along the first metal/air interface, partly scattered into air beyond the corner, and partly travels along the second metal/air interface.

The reflected signal is two orders of magnitude weaker in energy than the transmitted signal. The reflected signal weakens as the corner angle  $\alpha$  increases and vanishes for  $\alpha = 180^\circ$ . The energy of the signal scattered into air beyond the corner is inversely proportional to the distance from the corner except in a angular sector close to the second metal/air interface.

The intensity of the received signal at the second metal/air interface increases as either the corner angle  $\alpha$  increases and/or the carrier wavelength  $\lambda_c$  increases. However, the duration at a fixed point of reception on the second metal/air interface is approximately constant when  $\alpha$  is obtuse but decreases when  $\alpha$  is acute. The longer the signal propagates on the second metal/air interface, the larger is its duration. The shape of the received signal is largely independent of the corner angle of the corner and the carrier wavelength. Statistical analysis revealed that the signal after the concave corner is strongly and positively correlated with the transmitted signal, a promising result for SPP-wave-based optical interconnects. The received signal is better correlated with the transmitted signal when the carrier wavelength is lower for a fixed value of the corner angle.

Although our theoretical formulation allows us to consider metal/dielectric interfaces, we chose air as the dielectric material (and thereby eliminated dispersion as well as dissipation in one of the two partnering materials), so as to consider the essential characteristics of information transfer around a concave corner. We will present the more realistic case of metal/silicon interfaces in future publications.

## Acknowledgment

R. Agrahari thanks the Council of Scientific & Industrial Research (India) for financial assistance in the form of a CSIR NET JRF/SRF. A. Lakhtakia thanks the Charles Godfrey Binder Endowment at Penn State for ongoing support of his research activities.

## References

- [1] "Ultra-fast, energy-sipping devices powered by Intel." [Online]. Available: <https://www.intel.com/content/www/us/en/silicon-innovations/intel-14nm-technology.html>, Accessed on Aug. 4, 2018.
- [2] E. Ozbay, "Plasmonics: Merging photonics and electronics at nanoscale dimensions," *Science*, vol. 311, no. 5758, pp. 189–193, 2006.
- [3] J. S. Sekhon and S. S. Verma, "Plasmonics: The future wave of communication," *Current Sci.*, vol. 101, no. 4, pp. 484–488, 2011.
- [4] S. A. Maier, *Plasmonics: Fundamentals and Applications*. New York, NY, USA: Springer, 2007.
- [5] J. Homola, Ed., *Surface Plasmon Resonance Based Sensors*, Berlin, Germany: Springer, 2006.
- [6] J. A. Polo, Jr., T. G. Mackay, and A. Lakhtakia, *Electromagnetic Surface Waves: A Modern Perspective*. Waltham, MA, USA: Elsevier, 2013.
- [7] J. A. Conway, S. Sahni, and T. Szkopek, "Plasmonic interconnects versus conventional interconnects: A comparison of latency, crosstalk and energy costs," *Opt. Exp.*, vol. 15, no. 8, pp. 4474–4484, 2007.

- [8] R. Agrahari, A. Lakhtakia, and P. K. Jain, "Information carried by a surface-plasmon-polariton wave across a gap," *J. Appl. Phys.*, vol. 124, no. 5, 2018, Art. no. 053104.
- [9] J. L. Rodgers and W. A. Nicewander, "Thirteen ways to look at the correlation coefficient," *Amer. Statist.*, vol. 42, no. 1, pp. 59–66, 1988.
- [10] C. Kittel, *Introduction to Solid State Physics*, New Delhi, India: Wiley, 1974.
- [11] K. Wada, H.-C. Luan, D. R. Lim, and L. C. Kimerling, "On-chip interconnection beyond semiconductor roadmap: Silicon microphotonics," *Proc. SPIE*, vol. 4870, no. 1, pp. 437–444, 2002.
- [12] Y. A. Vlasov and S. J. McNabb, "Losses in single-mode silicon-on-insulator strip waveguides and bends," *Opt. Exp.*, vol. 12, no. 8, pp. 1622–1631, 2004.
- [13] K. S. Yee, "Numerical solution of initial boundary value problems involving Maxwell's equations in isotropic media," *IEEE Trans. Antennas Propag.*, vol. 14, no. 3, pp. 302–307, May 1966.
- [14] A. Z. Elsherbeni and V. Demir, *The Finite-Difference Time-Domain Method for Electromagnetics With MATLAB Simulations*, 2nd ed. Edison, NJ, USA: SciTech, 2016.
- [15] R. F. Oulton, D. F. P. Pile, Y. Liu, and X. Zhang, "Scattering of surface plasmon polaritons at abrupt surface interfaces: Implications for nanoscale cavities," *Phys. Rev. B*, vol. 66, no. 3, 2007, Art. no. 035408.
- [16] A. V. Novitsky, "Conversion from surface wave to surface wave on reflection," *J. Opt.*, vol. 12, no. 11, 2010, Art. no. 115705.
- [17] J. J. Foley IV, J. M. McMahon, G. C. Schatz, H. Harutyunyan, G. P. Wiederrecht, and S. K. Gray, "Inhomogeneous surface plasmon polaritons," *ACS Photon.*, vol. 1, no. 8, pp. 739–745, 2014.
- [18] F. Armin, M. Kordi, and M. M. Mirsalehi, "Propagation of surface plasmon modes through discontinuities," *Opt. Lett.*, vol. 43, no. 15, pp. 3754–3757, 2018.
- [19] J.-P. Berenger, "A perfectly matched layer for the absorption of electromagnetic waves," *J. Comput. Phys.*, vol. 114, no. 2, pp. 185–200, 1994.
- [20] M. F. Iskander, *Electromagnetic Fields and Waves*, 2nd ed. Long Grove, IL, USA: Waveland Press, 2013.
- [21] P. B. Johnson and R. W. Christy, "Optical constants of the noble metals," *Phys. Rev. B*, vol. 6, no. 12, pp. 4370–4379, 1972.
- [22] H. U. Yang, J. D'Archangel, M. L. Sundheimer, E. Tucker, G. D. Boreman, and M. B. Raschke, "Optical dielectric function of silver," *Phys. Rev. B*, vol. 91, no. 23, 2015, Art. no. 235137.
- [23] J. S. Walker, *Fourier Analysis*. New York, NY, USA: Oxford Univ. Press, 1988.
- [24] T. W. Körner, *Fourier Analysis*. Cambridge, U.K.: Cambridge Univ. Press, 1988.
- [25] S. C. Chapra and R. P. Canale, *Numerical Methods for Engineers*, 4th ed. New York, NY, USA: McGraw-Hill, 2002.
- [26] J. B. Geddes III and A. Lakhtakia, "Numerical investigation of reflection, refraction, and diffraction of pulsed optical beams by chiral sculptured thin films," *Opt. Commun.*, vol. 252, no. 4–6, pp. 307–320, 2005.
- [27] A. Lakhtakia, V. V. Varadan, and V. K. Varadan, "Scattering by periodic achiral–chiral interfaces," *J. Opt. Soc. Amer. A*, vol. 6, no. 11, pp. 1675–1681, 1989.
- [28] W. C. Chew, *Waves and Fields in Inhomogeneous Media*. New York, NY, USA: IEEE Press, 1999.